SCIENCE CHINA
Earth Sciences

• RESEARCH PAPER •

January 2014 Vol.57 No.1: 153–166
doi: 10.1007/s11430-013-4628-z

An improved CESE method and its application to steady-state coronal structure simulation

ZHOU YuFen* & FENG XueShang

SIGMA Weather Group, State Key Laboratory for Space Weather, Center for Space Science and Applied Research, Chinese Academy of Sciences, Beijing 100190, China

Received July 4, 2012; accepted February 22, 2013; published online June 17, 2013

This paper presents an improved space-time conservation element and solution element (CESE) method by applying a non-staggered space-time mesh system and simply improving the calculation of flow variables and applies it to magnetohydrodynamics (MHD) equations. The improved CESE method can improve the solution quality even with a large disparity in the Courant number (CFL) when using a fixed global marching time. Moreover, for a small CFL (say < 0.1), the method can significantly reduce the numerical dissipation and retain the solution quality, which are verified by two benchmark problems. And meanwhile, comparison with the original CESE scheme shows better resolution of the improved scheme results. Finally, we demonstrate its validation through the application of this method in three-dimensional coronal dynamical structure with dipole magnetic fields and measured solar surface magnetic fields as the initial input.

improved CESE scheme, numerical dissipation, steady-state coronal structure

Citation: Zhou Y F, Feng X S. 2014. An improved CESE method and its application to steady-state coronal structure simulation. Science China: Earth Sciences, 57: 153−166, doi: 10.1007/s11430-013-4628-z

The space-time conservation element and solution element (CESE) method, originally proposed by Chang (1995) and Chang et al. (1994, 1999), is a powerful numerical frame for solving conservation laws. This method is non-conventional by differing substantially from other well-established finite difference methods. The CESE method has many non-traditional features, including (1) a unified treatment of space and time, (2) introduction of conservation element and solution element for space-time flux conservation at interfaces, and (3) flow variables and their spatial derivatives as independent time-marching variables. The methodology consistently conforms to the conservation nature of the fluid physics, which conserves space-time fluxes both locally and globally in the solution domain. This characteristic can reduce the potential solution error when a non-conservative numerical method is applied. To date the CESE method has seen its great success in studying flows with moving and steady shocks, acoustic waves, complex vertical flows, detonations, shock/acoustics/vortices interactions, dam-break flows, solar wind, etc. (Chang et al., 1994, 1999; Wang et al., 1995, 1999; Zhang et al., 2006; Feng et al., 2006, 2007, 2010; Qamar et al., 2010).

The original CESE scheme that in two space dimensions strictly requires the use of structured/unstructured triangular meshes has been extended by Zhang et al. (2003, 2006) for the numerical solution of the ideal magnetohydrodynamics (MHD) equations using quadrilateral meshes. But the numerical dissipation associated with the CESE scheme increases as the Courant number (CFL) decreases. As a result, for a small CFL number (say < 0.1), a CESE scheme may become overly dissipative. And, in a case with a large CFL number disparity, the solution obtained by the CESE

*Corresponding author (email: yfzhou@spaceweather.ac.cn)

scheme can be subjected to severe numerical dissipation in a region where the local CFL number is far less than 1. This is caused by large grid-size disparity or small time step size (Yen et al., 2005, 2006; Venkatachari et al., 2008). In transient MHD simulations, the values of local CFL number may vary sharply across the computational domain using a fixed marching time step size. As a result, these values may range from its maximum stability bound, i.e., 1, to a far less than the value of 1, where the CESE method can become very dissipative. In order to overcome this disadvantage, Courant number insensitive scheme (CNIS) (Chang et al., 2003; Yen et al., 2005, 2006; Venkatachari et al., 2008) has been proposed to improve the solution quality, which can decrease numerical dissipation through improving the procedure for calculating the spatial derivatives.

In solar wind simulations, the grid points are accumulated heavily near the Sun due to the spherical shell geometry of the computational domain, and the plasma flow and magnetic field vary over many orders of magnitude in the solar-terrestrial space. This implies a large variation of the CFL stability limit from the corona to interplanetary space. Typically, the MHD time step is 1–3 s in the corona by the CFL criterion, and it will be 100–300 s in interplanetary space. If one uniform time step in the entire solar-terrestrial domain is applied, such distributions of mesh grids and physical parameters lead to a huge disparity in CFL across the mesh. Thus, making the numerical solution less insensitive to variation in CFL is necessary to get rid of the excessive numerical dissipation caused by small CFL and achieve a higher numerical accuracy.

In this paper, we propose an improved CESE scheme. The improved scheme can enhance the solution quality in a flow simulation with a large disparity in the CFL, and decrease numerical dissipation and retain the solution quality even if CFL is less than 0.1. Moreover, it is simple and easy to program, and does not need to improve the procedure for calculating the spatial derivatives. The original CESE scheme applied a staggered space-time mesh. In this improved scheme, we use a non-staggered space-time mesh. For verifying the accuracy, resolution, and efficiency of the improved scheme, we simulate two 2D benchmark problems, and conduct a comparative study between the improved CESE scheme and the original CESE scheme. Finally, we apply this method to simulate the three-dimensional coronal dynamical structure using dipole magnetic fields and measured solar surface magnetic fields as the initial input.

1 Numerical methods

In this section, we describe the improved CESE scheme on a two dimensional structured mesh, and it can decrease numerical dissipation and enhance the solution quality. The scheme can easily be extended to three dimensions and it could also be extended to unstructured meshes. The examples presented in the next section include two-dimensional benchmark test cases and three-dimensional coronal dynamical structure. Here, we will not introduce three-dimensional scheme.

1.1 Review of the CESE method

As a preliminary, we briefly review the existing 2D CESE method for the ideal MHD equations. In two spatial dimensions, the MHD equations can be cast into the following conservative form:

$$\frac{\partial \boldsymbol{U}}{\partial t}+\frac{\partial \boldsymbol{F}(\boldsymbol{U})}{\partial x}+\frac{\partial \boldsymbol{G}(\boldsymbol{U})}{\partial y}=0, \tag{1}$$

where $\boldsymbol{U}$ is the vector of conserved variables, $\boldsymbol{F}$ and $\boldsymbol{G}$ are the conservation flux vectors in the x and y directions respectively. These vectors are

$$\begin{aligned}\boldsymbol{U}&=(\rho,\rho u,\rho v,\rho w,e,B_x,B_y,B_z)^{\mathrm{T}}\\&=(u_1,u_2,u_3,u_4,u_5,u_6,u_7,u_8)^{\mathrm{T}}\end{aligned}$$

$$\boldsymbol{F}(\boldsymbol{U})=\begin{pmatrix}\rho u\\ \rho u^2+p_0-B_x^2\\ \rho uv-B_xB_y\\ \rho uw-B_xB_z\\ (e+p_0)u-B_x(\mathrm{u}\cdot\mathrm{B})\\ 0\\ uB_y-vB_x\\ uB_z-wB_x\end{pmatrix}=\begin{pmatrix}f_1\\ f_2\\ f_3\\ f_4\\ f_5\\ f_6\\ f_7\\ f_8\end{pmatrix},$$

$$\boldsymbol{G}(\boldsymbol{U})=\begin{pmatrix}\rho v\\ \rho vu-B_yB_x\\ \rho v^2+p_0-B_y^2\\ \rho vw-B_yB_z\\ (e+p_0)v-B_y(\mathrm{u}\cdot\mathrm{B})\\ vB_x-uB_y\\ 0\\ vB_z-wB_y\end{pmatrix}=\begin{pmatrix}g_1\\ g_2\\ g_3\\ g_4\\ g_5\\ g_6\\ g_7\\ g_8\end{pmatrix}. \tag{2}$$

Here, ρ and p are density and gas pressure, respectively; $\boldsymbol{u}$ = (u, v, w) and $\boldsymbol{B}$ = (B_x, B_y, B_z) are velocity components and magnetic field components in the x, y, z directions, respectively. The specific total energy e and the total pressure are $e = p/(\gamma - 1) + \rho\boldsymbol{u}^2/2 + \boldsymbol{B}^2/2$ and $p_0 = p + \boldsymbol{B}^2/2$, respectively.

In the following, we will briefly illustrate the CESE method based on the regular quadrilateral meshes in a two-dimensional space. For more detailed derivation, the reader can refer to Zhang et al. (2002). Let (x, y, t) be the coordinates of a three-dimensional Euclidean space E_3. By using

Gauss's divergence theorem in the space-time E_3, it can be shown that eq. (1) is equivalent to the following integral equations:

$$\oint_{S(V)} h_m \cdot \mathrm{d}S = 0, m = 1,\ 2, \cdots 8, \tag{3}$$

where m indicates the number of equations, $h_m = (f_m, g_m, u_m)$, $S(V)$ is the boundary of an arbitrary space-time region V in E_3. And $h_m \cdot \mathrm{d}S$ is the space-time flux h_m leaving the region V through the surface element $\mathrm{d}S$, where $\mathrm{d}S = \mathrm{d}\sigma n$ with $\mathrm{d}\sigma$ is the area of a surface element on $S(V)$, and n is the outward unit normal to S.

We firstly divide the x-y plane into non-overlapping uniform quadrilaterals and any two neighboring quadrilaterals share a common side (Figure 1(a)). The centroid of each quadrilateral is marked by either a hollow circle or a solid circle. Point Q, marked by a solid circle, is the centroid of a typical quadrilateral $B_1B_2B_3B_4$, and is also the centroid of polygon $A_1B_1A_2B_2A_3B_3A_4B_4$, which coincides with quadrilateral $A_1A_2A_3A_4$. The points A_ℓ, ℓ = 1, 2, 3, 4, marked by hollow circles, are the centroids of the four quadrilaterals neighboring to the quadrilateral $B_1B_2B_3B_4$, respectively. At each grid point, we construct one conservation element (CE) and one associated solution element (SE). The CE(Q) of point Q is defined to be the hexahedron $A_1A_2A_3A_4A'_1A'_2A'_3A'_4$. The SE($Q$) of point Q is defined as the union of the three plane segments $B_1'B_1'B_3'B_3''$, $B_2'B_2'B_4'B_4''$, and $A_1A_2A_3A_4$ and their immediate neighborhoods, see Figure 1(b). Let n be the index for t, for a given $n > 0$, Q, Q', and Q'', respectively, denote the points at the time level n, $n - 1/2$, and $n + 1/2$ with point Q (see Figure 1(b)) being their common spatial projection.

The solution of $(u_m)_Q$ can be obtained by solving the MHD equations on conservation element and solution element defined above. Following Chang's original approach (Chang et al., 1995, 1999), for any $(x, y, t) \in SE(Q)$, $u_m^*(x, y, t)$, $f_m^*(x, y, t)$, and $g_m^*(x, y, t)$, respectively, are approximated by the first-order Taylor series

$$u_m^*(x,y,t) = (u_m)_Q + (u_{mx})_Q(x - x_Q) + (u_{my})_Q(y - y_Q) + (u_{mt})_Q(t - t^n), \tag{4a}$$

$$\Gamma_m^*(x,y,t) = (\Gamma_m)_Q + (\Gamma_{mx})_Q(x - x_Q) + (\Gamma_{my})_Q(y - y_Q) + (\Gamma_{mt})_Q(t - t^n), \tag{4b}$$

where x_Q, y_Q, and t^n are the space-time coordinates of point Q, and Γ_m stands for f_m or g_m. By using chain rule, we have

$$(\Gamma_{mx})_Q = \sum_{\ell=1}^{8} (\Gamma_{m,\ell})_Q (u_{\ell x})_Q, \tag{5}$$

where $(\Gamma_{m,\ell})_Q$ is the element of the Jacobian matrices of Γ. It is similar for $(\Gamma_{my})_Q$ and $(\Gamma_{mt})_Q$. To proceed, by employing eq. (1), we have

$$(u_{mt})_Q = -\sum_{\ell=1}^{8} (f_{m,\ell})_Q (u_{\ell x})_Q - \sum_{\ell=1}^{8} (g_{m,\ell})_Q (u_{\ell y})_Q. \tag{6}$$

As a result, the flow variables $(u_m)_Q$ and their spatial gradients $(u_{mx})_Q$ and $(u_{my})_Q$ are the independent unknowns to be solved in the CESE method. Once these three variables are calculated, the flow solution structure inside the SE is completely determined.

Thus, the space-time flux conservation, eq. (3) can be approximated by its discrete counterpart on conservation element:

$$\oint_{S(CE)} h_m^* \cdot \mathrm{d}S = 0. \tag{7}$$

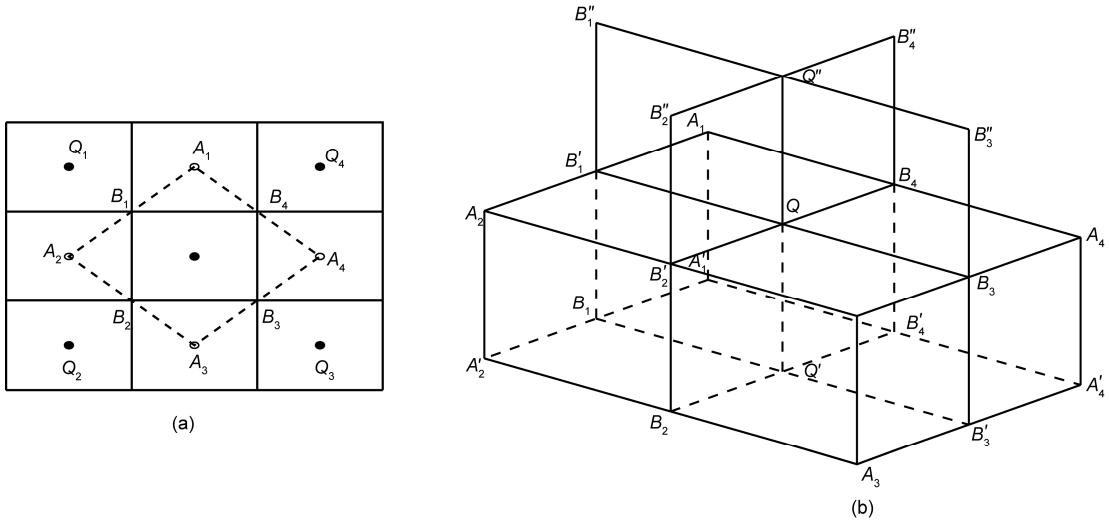

Figure 1 Space-time geometry of the CESE method. (a) Representative grid points in an x-y plane; (b) the definitions of CE and SE.

Then, substituting eqs. (4), (5) and (6) into eq. (7), we obtain the following equation:

$$\left(u_m\right)_Q^n = \sum_{\ell=1}^{4}\left(S^\ell R_{1m}^\ell - \frac{\Delta t}{2} R_{2m}^\ell \right) / S. \tag{8}$$

Here

$$R_{1m}^\ell = (u_m)_{A_\ell}^{n-1/2} + (x^\ell - x_{A_\ell})(u_{mx})_{A_\ell}^{n-1/2} + (y^\ell - y_{A_\ell})(u_{my})_{A_\ell}^{n-1/2}, \tag{9a}$$

$$\begin{aligned} R_{2m}^\ell = & \sum_{k=1}^{2} \lambda_k^\ell \left\{ n_{kx}^\ell \left[(f_m)_{A_\ell}^{n-1/2} + (x^\ell - x_{A_\ell})(f_{mx})_{A_\ell}^{n-1/2} \right.\right. \\ & \left.\left. + \frac{\Delta t}{4}(f_{mt})_{A_\ell}^{n-1/2} + (y^\ell - y_{A_\ell})(f_{my})_{A_\ell}^{n-1/2} \right] \right\} \\ & + \sum_{k=1}^{2} \lambda_k^\ell \left\{ n_{ky}^\ell \left[(g_m)_{A_\ell}^{n-1/2} + (x^\ell - x_{A_\ell})(g_{mx})_{A_\ell}^{n-1/2} \right.\right. \\ & \left.\left. + \frac{\Delta t}{4}(g_{mt})_{A_\ell}^{n-1/2} + (y^\ell - y_{A_\ell})(g_{my})_{A_\ell}^{n-1/2} \right] \right\}, \end{aligned} \tag{9b}$$

where S^ℓ, and $(x^\ell, y^\ell, t^{n-1/2})$ denote the areas and the coordinates of the centroids of the neighbor quadrilaterals, respectively. Thus, $S = \sum_{\ell=1}^{4} S^\ell$. λ_k^ℓ, $(n_{kx}^\ell, n_{ky}^\ell)$, and (x_k^ℓ, y_k^ℓ), respectively, denote the length, the unit outward normal, and the coordinates of the midpoint of the spatial projection of the (k, ℓ) side face which represents the eight side faces of CE(Q): $A_1'B_4'B_4A_1$, $A_1'B_1'B_1A_1$, $A_2'B_1'B_1A_2$, $A_2'B_2'B_2A_2$, $A_3'B_2'B_2A_3$, $A_3'B_3'B_3A_3$, $A_4'B_3'B_3A_4$, and $A_4'B_4'B_4A_4$, respectively.

A central difference type reconstruction approach is employed to calculate $(u_{mx})_Q$ and $(u_{my})_Q$, see Zhang et al. (2002) and Qamar et al. (2010). Using the Taylor series expansion in time only, we can obtain

$$(u_m')_{A_\ell}^n = (u_m)_{A_\ell}^{n-1/2} + \frac{\Delta t}{2}(u_{mt})_{A_\ell}^{n-1/2}. \tag{10}$$

By using the values of $(u_m)_{A_1}^n$, $(u_m)_{A_2}^n$ and $(u_m)_Q^n$, we can obtain the spatial derivatives $(u_{mx}^{(1)})_Q$ and $(u_{my}^{(1)})_Q$:

$$(u_{mx}^{(1)})_Q = \Delta_x / \Delta,\ (u_{my}^{(1)})_Q = \Delta_y / \Delta, \tag{11}$$

where

$$\Delta = \begin{vmatrix} \delta x_1 & \delta y_1 \\ \delta x_2 & \delta y_2 \end{vmatrix}, \Delta_x = \begin{vmatrix} \delta u_m^1 & \delta y_1 \\ \delta u_m^2 & \delta y_2 \end{vmatrix}, \Delta_y = \begin{vmatrix} \delta x_1 & \delta u_m^1 \\ \delta x_2 & \delta u_m^2 \end{vmatrix},$$

$$\delta u_m^\ell = (u_m')_{A_\ell}^n - (u_m)_Q^n, \delta x_\ell = x_{A_\ell} - x_Q, \delta y_\ell = y_{A_\ell} - y_Q.$$

Similarly, by using solutions at (A_2, A_3, Q), (A_3, A_4, Q) and (A_4, A_1, Q), we can get $(u_{mx}^{(2)})_Q$, $(u_{my}^{(2)})_Q$, $(u_{mx}^{(3)})_Q$, $(u_{my}^{(3)})_Q$, $(u_{mx}^{(4)})_Q$ and $(u_{my}^{(4)})_Q$, respectively. Finally, by using reweighting average, we can obtain the final flow variable gradients $(u_{mx})_Q$ and $(u_{my})_Q$ at Q, i.e.,

$$\left(u_{mx}\right)_Q = \begin{cases} 0, & \text{if } \theta_{mk} = 0, k = 1,2,\cdots 4, \\ \sum_{k=1}^{4}[(W_m^{(k)})^\alpha (u_{mx}^{(k)})_Q] / \sum_{k=1}^{4}(W_m^{(k)})^\alpha & \text{otherwise,} \end{cases} \tag{12a}$$

$$\left(u_{my}\right)_Q = \begin{cases} 0, & \text{if } \theta_{mk} = 0, k = 1,2,\cdots 4, \\ \sum_{k=1}^{4}[(W_m^{(k)})^\alpha (u_{my}^{(k)})_Q] / \sum_{k=1}^{4}(W_m^{(k)})^\alpha & \text{otherwise,} \end{cases} \tag{12b}$$

where

$$W_m^{(k)} = \prod_{\ell=1,\ell\neq k}^{4} \theta_{m\ell},\ \ \theta_{m\ell} = \sqrt{(u_{mx}^{(\ell)})^2 + (u_{my}^{(\ell)})^2},$$

where α is an adjustable constant (usually $\alpha = 1$ or $\alpha = 2$). To avoid dividing by zero, in practice a small positive number such as 10^{-60} is added to the denominators that appear in eq. (12a) and (12b).

1.2 The improved CESE scheme

Although the original CESE scheme is very successful in solving the above MHD equations, there is still room for improving the CESE method. For example, the numerical dissipation increases as the CFL number decreases. As a result, for a small CFL number (say < 0.1), the original CESE scheme may become overly dissipative. And when a globally fixed time step is used in a case with a large CFL number disparity, the CESE scheme can become very dissipative in a region where the local CFL number is far less than 1. In order to overcome this weakness, in this subsection, we propose an improved CESE scheme, which can enhance the solution quality even in a flow simulation with a large disparity in the CFL, and significantly decrease numerical dissipation and retain the solution quality even if CFL is less than 0.1. To proceed, we firstly propose the non-staggered extension of the original CESE scheme in the following.

The original 2D CESE scheme is based on structured/unstructured staggered space-time meshes. Wang et al. (1999) extended the 2D CESE scheme for unstructured triangular meshes using the non-staggered version. In this paper, we extend the original 2D CESE scheme to the case of regular quadrilateral non-staggered space-time meshes. In a manner similar to the case in Wang et al. (1999), the non-staggered mesh can be obtained by overlaying two previous staggered meshes. The calculation of u_m in the

non-staggered extension is the same as the original CESE scheme, and a similar statement does not hold.

Previously in the original CESE scheme, at one time level, assume the solutions at solid circles are obtained by using the hollow circles, and at the next time level, the solutions at hollow circles are obtained by using the solid circles. The non-staggered extension of the original staggered CESE scheme can be made in the following manner. At time $t^{n-1/2}$, assume the data are known at both solid and hollow circles. At time t^n, obtain the solutions at solid circles by using the hollow circles, and the solutions at hollow circles by using the solid circles. Thus for the non-staggered extension, as the solutions at the all meshes at time t^n have been obtained, the values of the derivative at time t^n can be straightly obtained by eq. (12), and do not need the Taylor series expansion in time by eq. (10). Such a calculation of derivatives u_{mx} and u_{my} is simpler. The key difference between the extension and the original CESE scheme is that the all meshes can be simultaneously computed in the non-staggered extension.

To reduce numerical dissipation for the original CESE scheme when CFL is small, we propose an improved CESE scheme based on the non-staggered extension by employing a start-off value σ. The quantity R_{1m}^{ℓ} in eq. (8) is replaced by $\sigma R_{1m}^{\ell}+(1-\sigma)u_m^{n-1/2}$. The resulting eq. (8) becomes

$$(u_m)_Q^n=(1-\sigma)(u_m)_Q^{n-1/2}+\left(\sigma\sum_{\ell=1}^{4}S^{\ell}R_{1m}^{\ell}-\frac{\Delta t}{2}\sum_{\ell=1}^{4}R_{2m}^{\ell}\right)/S, \tag{13}$$

where σ represents the local grid CFL number at Q. For calculating the local CFL number σ, we use a simplified grid CFL calculation as proposed by Yen et al. (2006). As the solutions at point Q and its surrounding points at time t^n have been obtained, the two spatial derivatives $(u_{mx})_Q$, and $(u_{my})_Q$ can be straightly obtained by eq. (12), which do not need to calculate the values of the surrounding points at time t^n by Taylor series expansion in time. Thus the combination of eq. (13) and eq. (12) constitutes the improved CESE scheme.

2 Results and discussion

In this section, in order to test the improved CESE scheme, two benchmark test cases, including isentropic stationary vortex and Orszag-Tang MHD turbulence, are chosen to simulate, and the comparison with the original CESE scheme is also made. To illustrate the application of the improved CESE method to stead-state coronal structure, three-dimensional coronal dynamical structure with dipole magnetic fields and measured solar surface magnetic fields as the initial input is simulated and presented herein. In the following numerical examples, we choose the adjustable constant $\alpha = 0$ for the first example and $\alpha = 1$ for the other examples.

2.1 Isentropic stationary vortex problem

The first numerical test is a 2D isentropic, stationary vortex embedded in a static environment (Yee et al., 1999). The benchmark test case is often used to assess the numerical dissipation error of numerical methods. Similar test cases have also been used by several authors for testing other schemes (Gottlieb et al., 1976; Davoudzadeh et al., 1995). In this test case, two velocity components (u, v) and temperature (T) are perturbed by the following values:

$$(\delta u,\delta v)=\frac{\beta}{2\pi}\mathrm{e}^{(1-r^2)/2}(-\bar{y},\bar{x}),\delta T=-\frac{(\gamma-1)\beta^2}{8\gamma\pi^2}\mathrm{e}^{1-r^2},$$

$$(\bar{x},\bar{y})=(x-x_0,y-y_0),r^2=(\bar{x}^2+\bar{y}^2),$$

where β is the vortex strength, x_0 and y_0 are the initial coordinates of the vortex center, and $\gamma = 1.4$. The computational domain is $(x \times y) \in [0, 50] \times [-5, 5]$, and two quadrilateral meshes (401 × 81 and 801 × 161) are used. The vortex is placed at the center of the rectangle, (25, 0). Periodic boundary conditions in both directions are used for this case. For this calculation, the global CFL number is set to a fixed value 0.8.

In order to assess order of accuracy of the present method for the smooth flows, the case is run on a sequence of successively finer uniform grids. The computed solutions are compared with the exact solution in order to calculate the L1 error norm. The resulting area-averaged L1 error norm at $t = 100$ is shown in Figure 2. The quantity N in the figure is the number of points in the y directions for the corresponding uniform mesh. When the grid size is doubled, the error norm decreases by roughly a factor 13 or better. This error norm confirms that the present method converges approximately at a four order rate for smooth solutions. Although not shown here, the original CESE scheme produces similar error norm convergence to the present

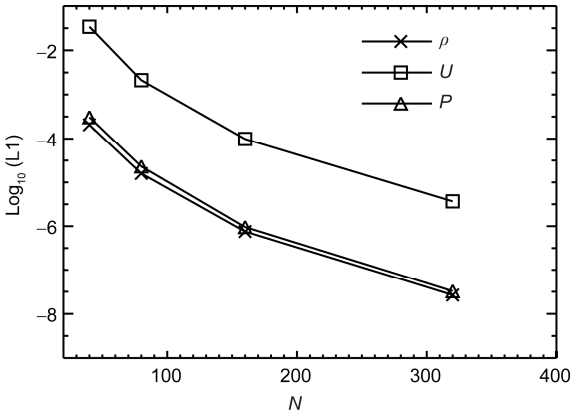

Figure 2 Convergence of error norm versus number of points for isentropic stationary vortex problem.

scheme.

In order to compare the original CESE scheme and the improved CESE scheme, the two approaches are evaluated in this study. Density profiles at the centerline, $y = 0$, cutting through the center of the vortex of the two schemes are used for comparison. Figure 3 shows the density profiles across the vortex at the centerline, $y = 0$, at $t = 50$ and 100 for the two schemes. Data on the centerline are extracted up to 5 unit lengths away to the left and the right, from the location of the center of the vortex. The solid lines represent the exact solution. The results show that the original CESE scheme gives some dissipation error near the center of the vortex for the coarser mesh at $t = 50$, and the fine quadrilateral mesh has minor dissipation error. At a later time $t = 100$, the computed vortex core of the original CESE scheme is even more diffused compared with the exact solution. The results of the improved CESE scheme match well with the analytical solution. For the fine mesh, the results of the improved CESE scheme have almost not diffused the vortex core, and all numerical solutions fall almost on top of the exact solution. Anyway, the improved CESE scheme exhibits its better resolution than the original CESE scheme. The results further suggest that the improved CESE scheme appears to perform much better than the original scheme for this case.

2.2 The Orszag-Tang MHD turbulence problem

In this problem, we consider the evolution of a compressible MHD vortex system by Orszag et al. (1979). It contains many significant features of MHD turbulence and has been studied by many previous investigators (Zhang et al., 2006; Qamar et al., 2010; Jiang et al., 2010). The computational domain in this case is $(x, y) \in [0, 2\pi] \times [0, 2\pi]$ with periodic boundary on all four sides. We use a uniform mesh of 200 × 200 grid nodes. The initial data are

$$\rho(x, y, 0) = \gamma^2, p(x, y, 0) = \gamma,$$
$$u(x, y, 0) = -\sin y, v(x, y, 0) = \sin x, w(x, y, 0) = 0,$$
$$B_x(x, y, 0) = -\sin y, B_y(x, y, 0) = \sin 2x, B_z(x, y, 0) = 0,$$

where $\gamma = 5/3$. The global CFL number is set to 0.8.

The Orszag-Tang vortex problem starts from smooth initial data, but gradually the flow becomes very complex as expected from a transition towards turbulence. Figure 4 shows the pressure contours of the present CESE results at t=0.5, 2 and 3, respectively. To assess the accuracy of the present results, the employed contour levels are exactly the same as that used by Jiang et al. (1999), i.e., 12 equally spaced contour levels ranging from 1.0 to 5.8 for $t = 0.5$, from 0.14 to 6.9 for $t = 2$, and from 0.36 to 6.3 for $t = 3$. From the results, we can see that there is no obvious difference between the present results and Jiang and Wu's results by side-by-side comparisons.

To test solution accuracy, the numerical errors at $t = 3$ are also calculated. Since the exact solution is not known, a high resolution numerical solution is used as a basis for

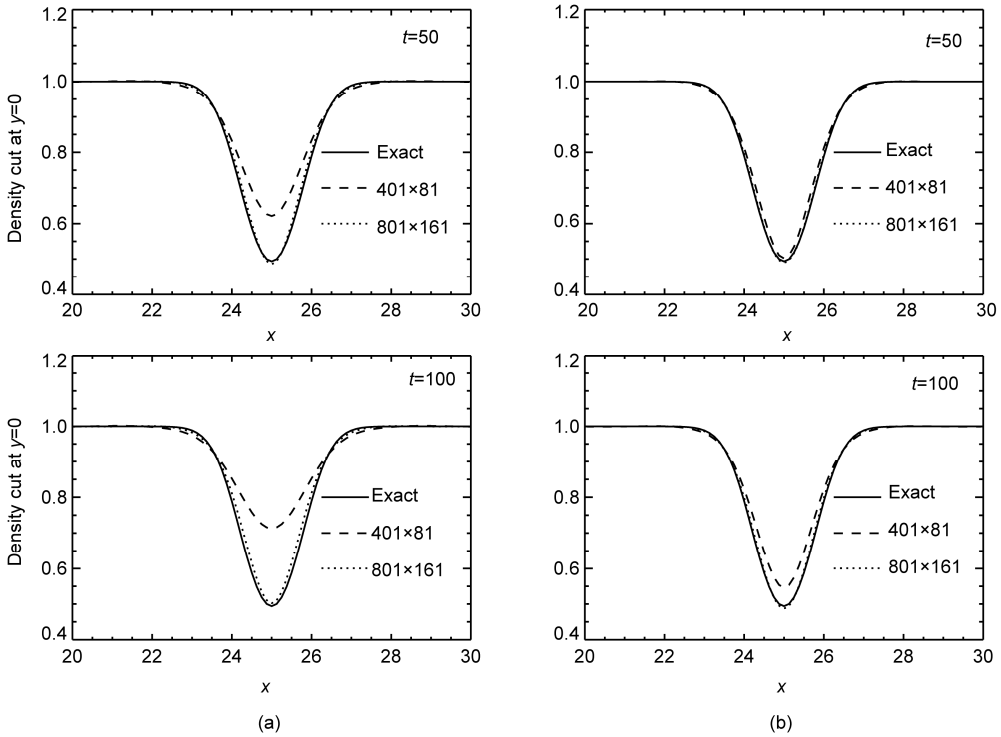

Figure 3 Comparison of the two methods with the exact solution, illustrated by density profiles at the centerline $y = 0$, at $t = 50$ and $t = 100$ for 401×81 grid and 801×161 grid. (a) The original CESE scheme; (b) the improved CESE scheme.

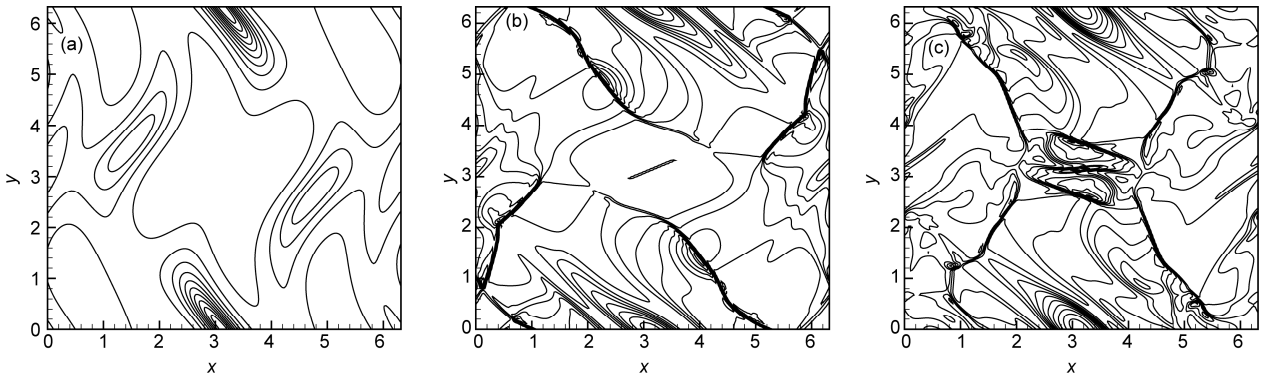

Figure 4 Pressure contours of the Orszag-Tang vortex problem by the improved CESE scheme. (a) Pressure contours at $t = 0.5$; (b) pressure contours at $t = 2$; (c) pressure contours at $t = 3$.

comparison. Here, the reference high resolution solution is obtained with the original CESE scheme on an $N \times N = 800 \times 800$ grid. Figure 5 shows the computed L1 error norm versus number of points used. The quantity N in the figure is the number of points in both the x and y directions for the corresponding uniform mesh. From the rate of change of the curve, the solution is approaching three orders.

For a comparison of the two schemes: the original scheme and the improved scheme, the qualitative differences in resolution can be appreciated in the gray scale images of pressure at $t = 3$ in Figure 6. The right of the figure is the reference high resolution numerical solution on an $N \times N = 800 \times 800$ grid via the original CESE scheme. The other two plots are results of two schemes with 200×200 resolution. Only the left of the computational domain is shown since the right half is symmetric to the center point $x = y = \pi$. The figure shows that the result of the improved CESE scheme is obviously sharper than that of the original CESE scheme. The improved CESE scheme shows clearly the sharp dark feature between $x = y = 1$ and $x = 0.5$, $y = 2$, which is obvious in the high resolution solution. But the feature is obscure in the solution from the original CESE scheme owing to the numerical dissipation.

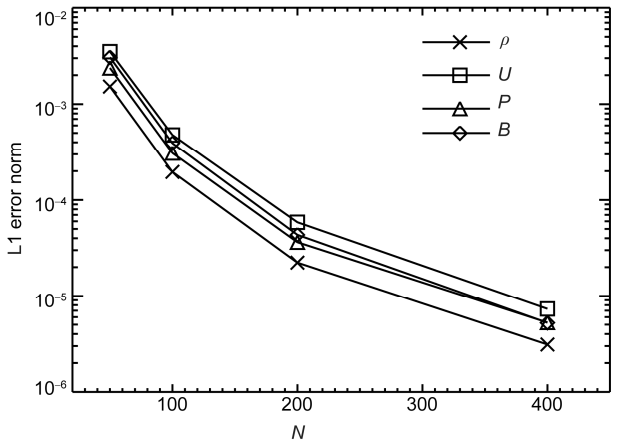

Figure 5 L1 error norm versus grid resolution for the Orszag-Tang MHD turbulence problem.

For quantitative details of the calculated results, Figure 7 shows the pressure profiles along the line of $y = 0.625\pi$ at time $t = 0.5$, 2 and 3, calculated by using the two schemes. The solid line represents the reference high resolution solution. At time $t = 0.5$, the flow is still quite smooth, and no discontinuities are present. There is no difference between the results of the two schemes and the reference high resolution solution. When calculated to $t = 2$, the result by the improved scheme shows a more pronounced gradient near $x = 0.3$ and $x = 3.5$, where obvious shock waves have been generated as the vortex system evolving (Figure 4(b)). At near $x = 5.5$, it can be seen that the improved scheme solution agrees well with the high resolution solution. However, the original CESE scheme solution shows deviation. At $t = 3$, when discontinuities and complicated flow interactions have formed, some differences could be discerned between $x = 0.5$ and $x = 1$. The result of the improved scheme is much closer to the high resolution solution, which has been mentioned above. Small differences could also be discerned at near $x = 1.6$ and $x = 4.4$, where strong shock discontinuities formed (Figure 4(c)), and the results of the original scheme are much smoother than that of the improved scheme due to the numerical dissipation. From these results, we found that the improved scheme can indeed enhance the accuracy of the solution. Due to the use of uniform grids, benefits of the improved scheme over the original scheme are not evident here.

To contrast the dissipative character at low CFL condition (say < 0.1), we calculate this case with CFL=0.08. Figure 8(a) and (b) shows the pressure contours of this problem solved by these two methods with CFL=0.08 at $t = 3$. The employed contour levels are also exactly the same as that used by Jiang et al. (1999). Figure 8(c) shows the corresponding pressure profiles of the two schemes along the line of $y = 0.625\pi$. The solid line also represents the reference high resolution solution, which is the same as that of the previous paragraph. From the results shown, it is clear that the original CESE solutions deteriorate quickly and do not capture the shock effectively when the global CFL

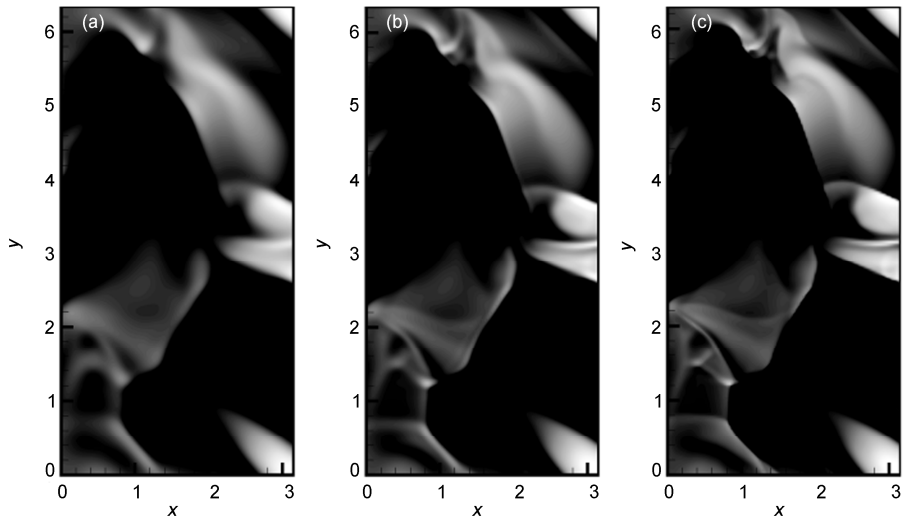

Figure 6 The pressure distribution in the Orszag-Tang vortex problem. The two schemes are computed at a 200 × 200 resolution. (a) The original CESE scheme; (b) the improved CESE scheme. The reference high resolution solution (c) is computed on an 800×800 grid.

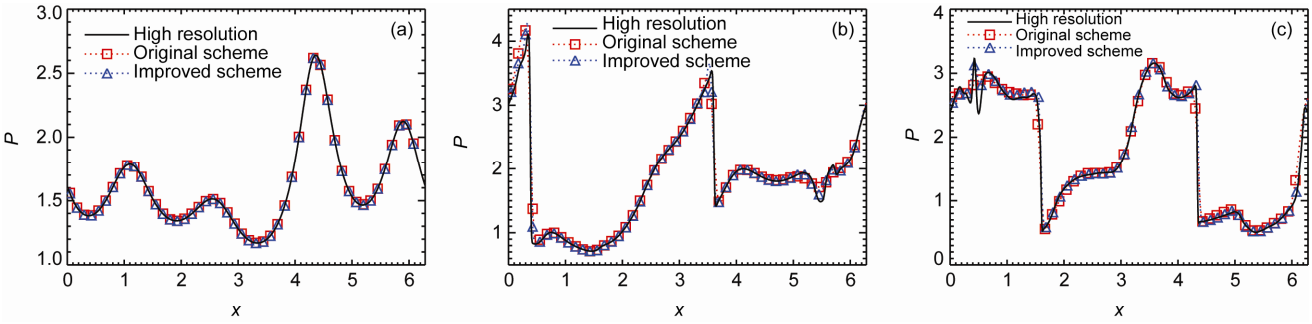

Figure 7 Pressure profile of the Orszag-Tang vortex problem along line $y = 0.625\pi$. (a) Pressure profile at $t = 0.5$; (b) pressure profile at $t = 2$; (c) pressure profile at $t = 3$.

number is less than 0.1. The solutions of the present method are still quite accurate even if CFL number < 0.1. The advantage of the present method over the original CESE method is overwhelming.

2.3 Three-dimensional steady state solar wind simulation using dipole magnetic field as an input

In this subsection, a benchmark example of a three-dimensional steady state coronal atmospheric problem is chosen by using dipole magnetic field as an input. This particular problem has been solved by many different methods; it allows us to test the newly improved scheme. The time-dependent MHD simulation code used in this section is similar to that described in Feng et al. (2007), in addition to the improved CESE scheme instead of the original CESE scheme. To initiate this numerical experiment, we choose a dipolar magnetic field and Parker's solar wind solution (Hundhausen et al., 1972) as the input. The dipole magnetic field is given by

$$B_r = 2B_0 \frac{R_s^3 \cos\theta}{r^3},\ B_\theta = B_0 \frac{R_s^3 \sin\theta}{r^3},$$

where R_s is the solar radius, and B_0 is the constant magnetic strength. The plasma beta is defined as $\beta = 16\pi nkT/B^2$, with k being Boltman constant. In this paper, we numerically test the present method for $\beta = 0.1$. The temperature and proton number density at the inner boundary are typically taken to be 1.8×10^6 K and 1×10^{14} m^{-3}. The specific heat ratio γ is assumed to be 1.05. The computational domain covers $-90° \leqslant \theta \leqslant 90°$, $0° \leqslant \phi \leqslant 360°$, and $1R_s \leqslant r \leqslant 30R_s$. The details of computing the background solar wind were given by us (Hundhausen et al., 1972) and thus are omitted here.

We numerically test the present method. After we input the chosen magnetic field and Parker's solar wind solution (Hundhausen et al., 1972), we run the numerical code with the use of 20 MPI processes and allow it to reach a steady-state solution at the physical time 100 h via the relaxation technique (Steinolfson et al., 1982). The present

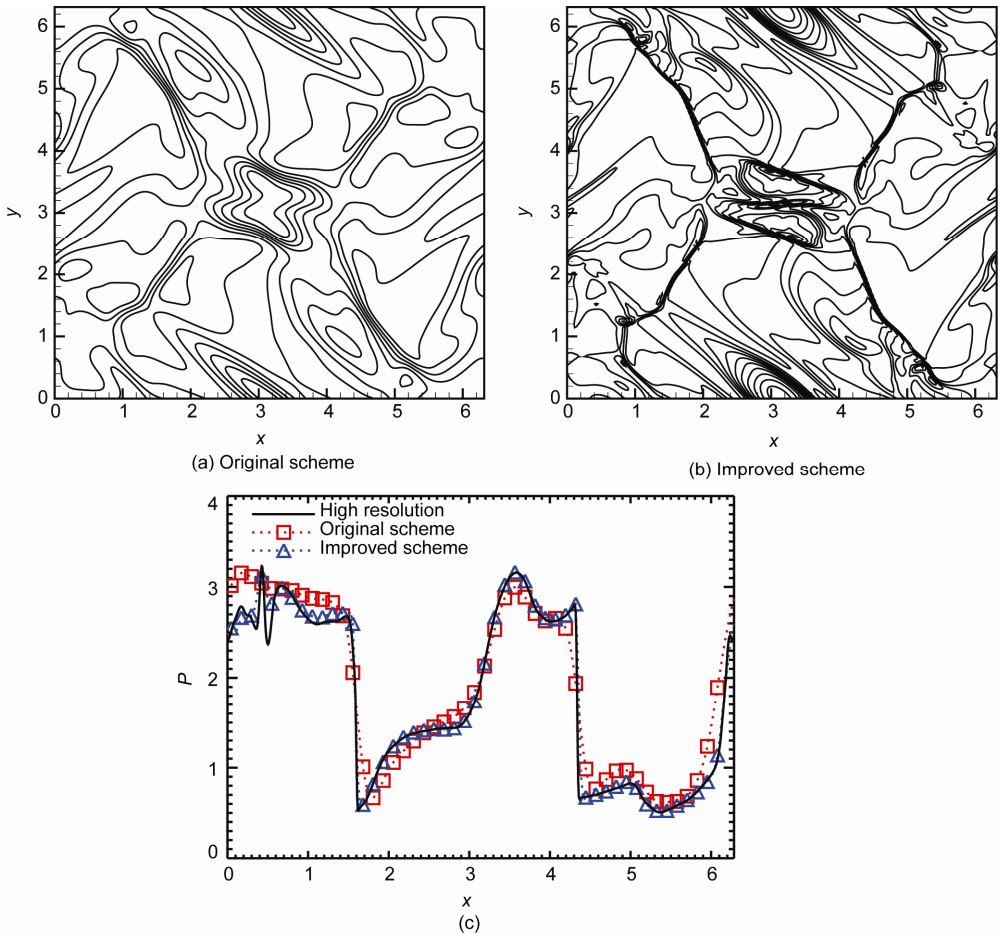

Figure 8 (a) and (b) Pressure contours of the Orszag-Tang vortex problem by the two schemes; (c) pressure profile of the Orszag-Tang vortex problem along line $y = 0.625\pi$ (CFL number= 0.08).

method takes about 35 h of wall time to obtain the steady-state solution. But its runtime is approximately 1.6 times as that of the original CESE method; this is caused by computational cost due to non-staggered extension and the grid CFL calculation. However, for a higher accuracy of the solution, the cost is worth it. Figure 9 depicts a two-dimensional (2-D) cut through the 3-D steady-state model in the meridional plane close to the Sun. The false color image indicates the radial speed of the plasma whereas the magnetic field is represented by solid black lines. The magnetic field remains closed at low latitude close to the Sun forming a streamer belt. At high latitude, the magnetic field is carried out with the solar wind to achieve an open configuration.

Figure 10 shows the profiles of proton number density, and the radial velocity vs. heliocentric distance at two different latitudinal angles: $\theta = 88°$ and $\theta = 2°$, which correspond, respectively, to the open field and current sheet region. The black lines represent the results of the present method. From these results, we recognize that the proton number density decreases with increasing of heliocentric distance, becoming smaller toward the polar region. This picture agrees with the observed magnetic field topology of

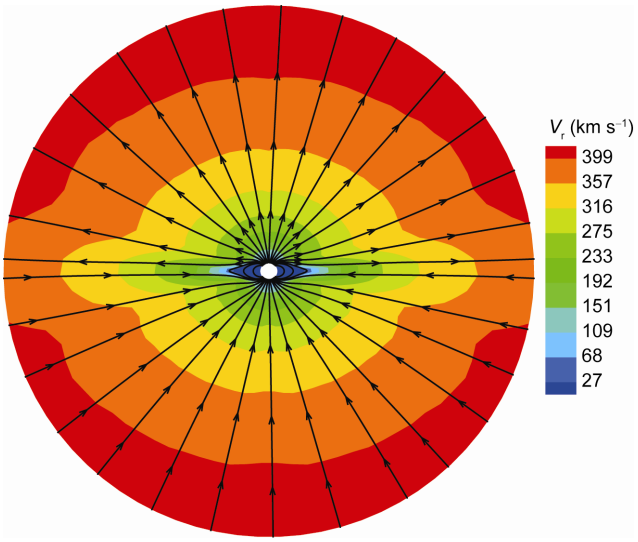

Figure 9 Magnetic field and radial speed for the steady state solar wind solution from $1R_s$ to $20R_s$. The color contours represent the radial speed and streamlines denote the magnetic field lines.

a coronal streamer at solar minimum (Sheeley et al., 1997). This configuration is due to the interaction between the

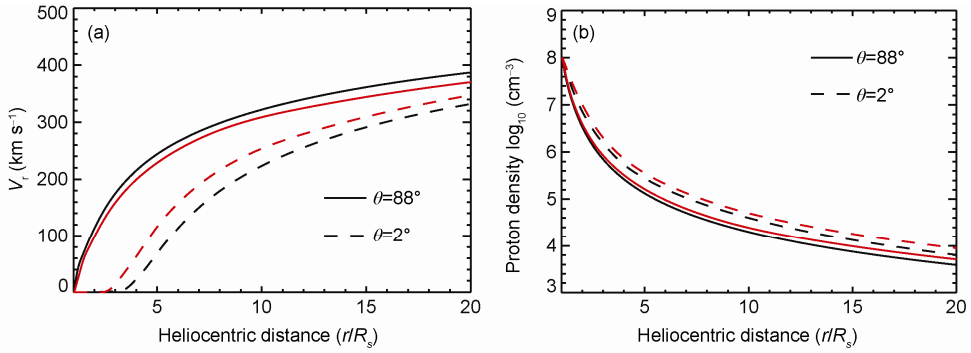

Figure 10 (a) Radial velocity profiles vs. heliocentric distance at two different latitude $\theta = 88°$ and $\theta = 2°$ and (b) the corresponding number density distributions. The black lines represent the results of the present method, and the red lines denote the results of the original CESE method.

magnetic field and Parker's radial solar wind solution. We also show that the radial velocity is higher at the polar region and increases in the radial direction. All these characteristics are consistent with previous solutions (Steinolfson et al., 1982; Wang et al., 1993; Zhang et al., 1993). The density structure in our simulation qualitatively agrees both with the fact that coronal streamer centers are formed around the solar equator, and with the MK III observations of coronal polarized brightness near solar minimum (Biesecker et al., 1999). The radial profile of bulk speed is not exactly consistent with measurements of flow speeds in the corona between 2 and 22 R_s (Sheeley et al., 1997), and this is because the polytropic calculation yields a rather slow bulk flow.

In order to make comparison between the present method and the original CESE method, we also run this case using the original CESE method. The results of the original CESE method are showed in Figure 10 by red lines. From these results in Figure 10, we found that the radial velocity of the present method is higher than that of the original CESE method at the open field region, and the radial velocity difference of the present method is greater. These are caused by the numerical dissipation of the original CESE method with the disparity in grid CFL number when using a fixed global marching time. From the Sun to $20R_s$, where the solar wind flow is essentially superfast (hence super-Alfvénic), the plasma flow and magnetic field vary over many orders of magnitude. Such distributions of physical parameters lead to a huge disparity in grid CFL from the Sun to $20R_s$ when using one uniform time step. For example, when reaching the steady state, from the Sun to $20R_s$, the local grid CFL can range from 0.8 to less than 0.01 in the simulation.

2.4 Three-dimensional coronal streamer structure simulation using measured photospheric magnetic field as an input

After three benchmark tests, we are ready to construct the approximate, realistic three-dimensional coronal atmospheric solutions to test the present numerical scheme. The prescribed initial magnetic field is based on measurements of the solar surface together with a potential field model. The measured photospheric magnetic field for Carrington rotation 1922 from the Wilcox Solar Observatory at Stanford University (http://wso.stanford.edu/synoptic.html) is used as the initial boundary condition to deduce a three-dimensional global potential magnetic field. We input this three-dimensional magnetic field model into the numerical code together with the assumed plasma properties (number density and temperature) and Parker's solar wind solution to allow the numerical code to arrive at a quasi-equilibrium solution via the relaxation method. In order to obtain a reasonable agreement with observed solar wind velocity, the heating form as in Zhou et al. (2012) is used here. The specific heat ratio γ is assumed to be 1.46.

In the following, we present the 3D numerical results of structured solar wind for CR 1922. Figure 11 shows the magnetic field lines and radial velocity on two different meridional planes. The figure shows that the magnetic field is characteristic of the heliospheric magnetic field during periods of solar minimum. At high latitudes, the magnetic field lines are carried out with the solar wind to form coronal holes of high speed. However, at lower latitudes around the equator, the magnetic field lines remain closed close to the Sun forming a streamer belt. Above the streamer, we can see a thin current sheet between different magnetic polarities. This scenario of the helmet streamer-current sheet system is consistent with those depicted by Pneuman et al. (1971) and Gosling et al. (1981). Inspection reveals a bimodal outflow pattern with slow wind leaving the Sun below 400 km s^{-1} near the equator and high-speed wind above 600 km s^{-1} found above 30 latitude.

Figure 12 displays the space weather background synoptic maps for the MHD steady-state solution on the different solar surfaces at $2.5R_s$ and $20R_s$. This configuration is due to the interaction between the magnetic field and Parker's solar wind flow field. Quantitatively, N and T decrease with heliocentric distance while V_r increases. The flow in the polar regions is faster than that near the equatorial regions,

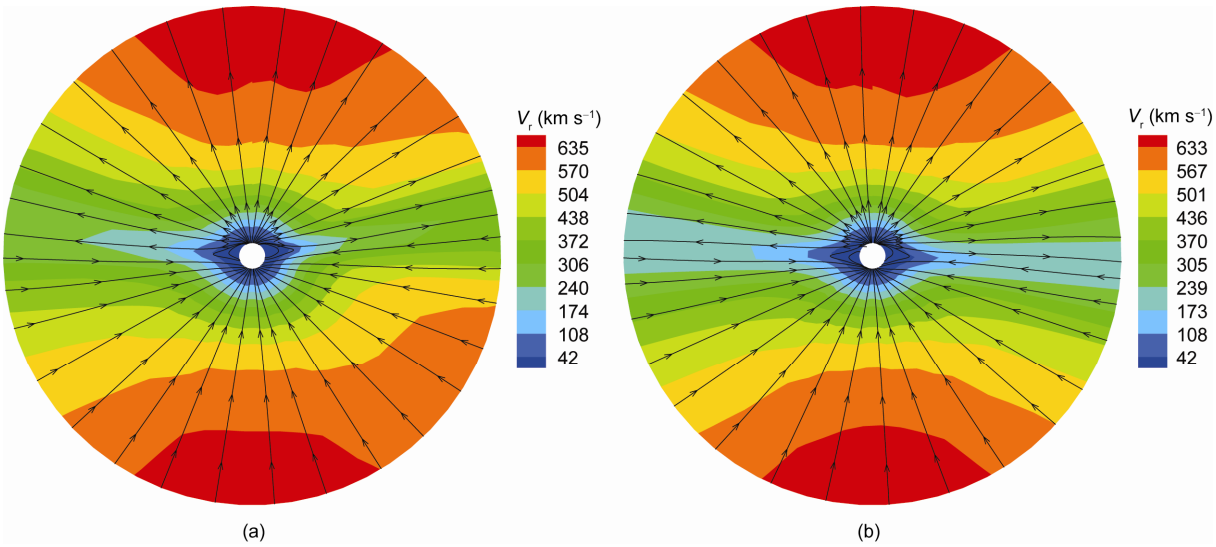

Figure 11 Magnetic field and radial speed for the steady state solar wind solution on the meridional planes at $\phi = 180°–0°$ and $\phi = 270°–90°$ from $1R_s$ to $20R_s$. The color contours represent the radial speed and streamlines denote the magnetic field lines.

and the heliosphere current sheet (HCS) region is surrounded by higher N. By examining the number density and velocity at $2.5R_s$ and $20R_s$, we found that these values of the number density are of the same order of magnitude as those results shown in Figure 1 of Wei et al. (2003) for the averaged distribution of the solar plasma number density n on the surface at $2.5R_s$, estimated from K coronal brightness during the Carrington rotations 1733–1742 in 1983, and the radial velocity at $2.5R_s$ is consistent with the averaged distribution of solar wind speed on the surface at $2.5R_s$ calculated from the mapping of interplanetary scintillation data during the Carrington rotation 1733–1742 in 1983, and also with results using data for Carrington rotation 1742 in 1983 in a special MHD method by Wei et al. (2003). Meanwhile, we noticed that the low-density regions have higher radial speed, which indicates that there exists a north polar coronal hole, a south polar coronal hole, and an equatorial structured distribution as a function of heliographic longitude. In a word, the numerical results for CR 1922 exhibit many properties typical of coronal atmospheric observations near solar minimum. The magnetic field strength falls off along with heliocentric distance, but less than the potential field model, which is proportional to $1/r^2$.

Figure 13 displays the radial velocity, and number density profiles along heliocentric distance at two different latitudes: $\theta = 88°$ and $\theta = 2°$ at the same longitude $\phi = 0°$, which corresponds, respectively, to the open field and the current sheet region. Evidently, we have a high-speed and low-density stream in the polar region. At $10R_s$ and above, the flow is super-Alfvénic and supersonic nearly everywhere and changes very little. However, a low speed and high-density flow is present in the current sheet region and the velocity agrees with the profile of low solar wind speed (Sheeley et al., 1997). Figure 14 shows the meridional profiles of the radial velocity, number density, radial magnetic field, and temperature at $\phi = 0°$.

In this paper, our results indicate that this model matches many features of the corona (as shown above) through considering an additional coronal heating input related to the expansion factor. So far the entire scenario for the coronal heating/solar wind acceleration is still unknown. To further understand this problem, more observations of multiple spacecraft (such as SDO, STEREO, SOHO, ACE, Wind, or other future missions) will probably help us develop the ability of including physically realistic coronal heating modules into 3D MHD codes; actually there have been many 2D counterpart studies using somewhat-physically-based coronal heating and wind acceleration mechanisms in the literature (e.g., Chen et al., 2001; Hu et al., 2003; Li et al., 2004). And more observations of multiple spacecraft can also help us improve the determination of the structure of the ambient solar wind, and further numerically characterize the 3D propagation of CMEs through the heliosphere. This point is left for future consideration.

3 Conclusions

In the study, an improved CESE scheme is proposed and applied to MHD equations. The improved CESE scheme can enhance the accuracy of the solution with a large disparity in the grid CFL when a globally fixed time step is used. Moreover, the scheme can significantly reduce the numerical dissipation and retain the solution quality when CFL number is less than 0.1. The present scheme is very simple and easy to program. In order to construct the present scheme, we firstly extend the original CESE scheme, which is based on staggered space-time meshes to the case

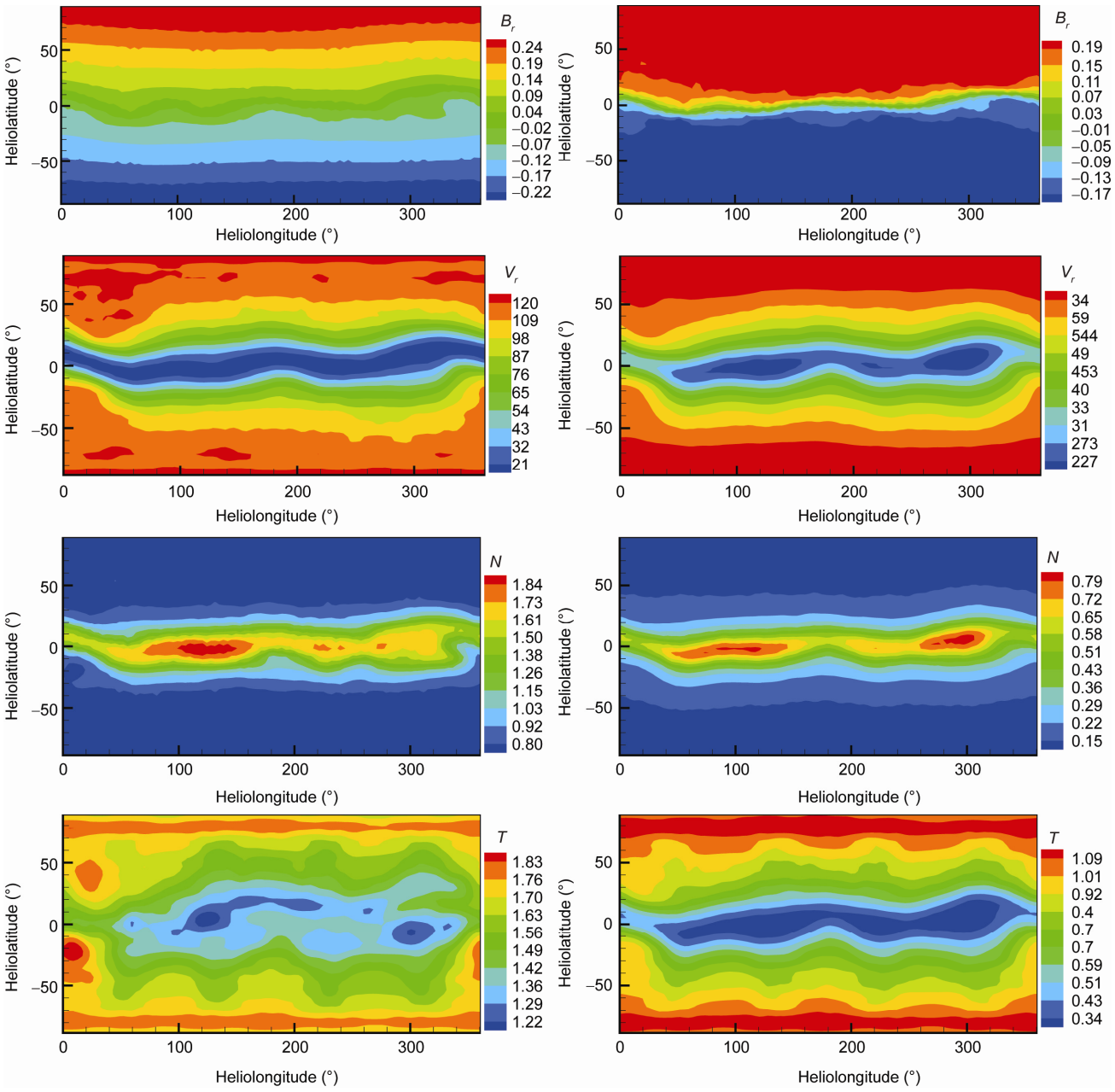

Figure 12 Contours of MHD steady-state solution on the difference surface at $2.5R_s$ (left column), $20R_s$ (right column). The top panel denotes radial magnetic field B_r with units Gauss, and 10^{-6} T from left to right; the second panel is the radial speed with units km s^{-1}; the third panel displays the number density with units 10^6 cm^{-3}, and 10^4 cm^{-3} from left to right; the bottom panel stands for temperature with units 10^6 K.

of non-staggered space-time meshes. Based on the non-staggered extension, we propose the improved CESE scheme. In the present scheme, at the new time, we obtain the solutions at all meshes using the data at the previous time. Meanwhile, the derivatives calculation is simplified, which does not need to calculate the value at neighbor meshes using the Taylor series expansion.

Generally, a careful control of numerical dissipation is a necessity for an accurate and stable steady simulation, as well as for an unsteady simulation, but it is difficult to properly control numerical dissipation. Although one can increase the numerical dissipation rather easily for a numerical scheme, it is much harder to reduce it when accuracy is required. Though the original CESE scheme can reduce numerical dissipative scheme with the adjustable constant α, it may become very dissipative when CFL is small. Here, the improved scheme makes it easier to reduce numerical dissipation.

For verifying the accuracy, and efficiency of the present scheme, firstly two 2D benchmark problems are simulated, including isentropic stationary vortex and Orszag-Tang MHD turbulence problem. Solution accuracy of this present

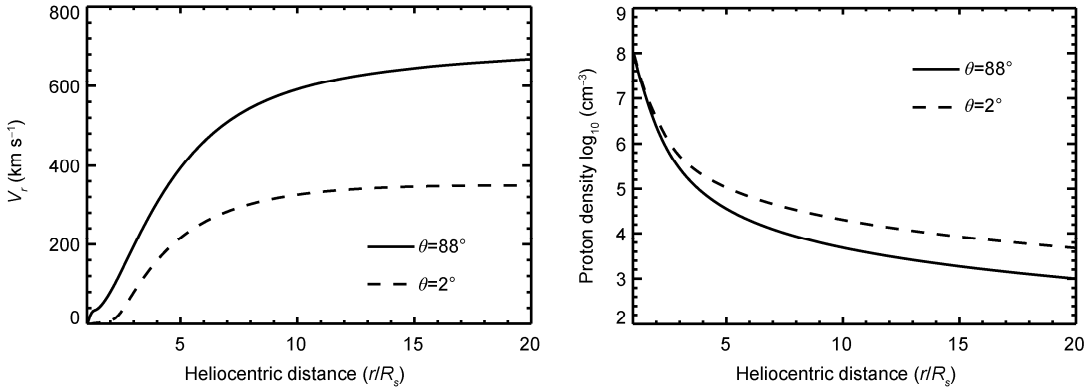

Figure 13 Profiles of the radial velocity, and number density at two locations with different latitude $\theta = 88°$ and $\theta = 2°$ at the same Carrington longitude $\phi = 0°$.

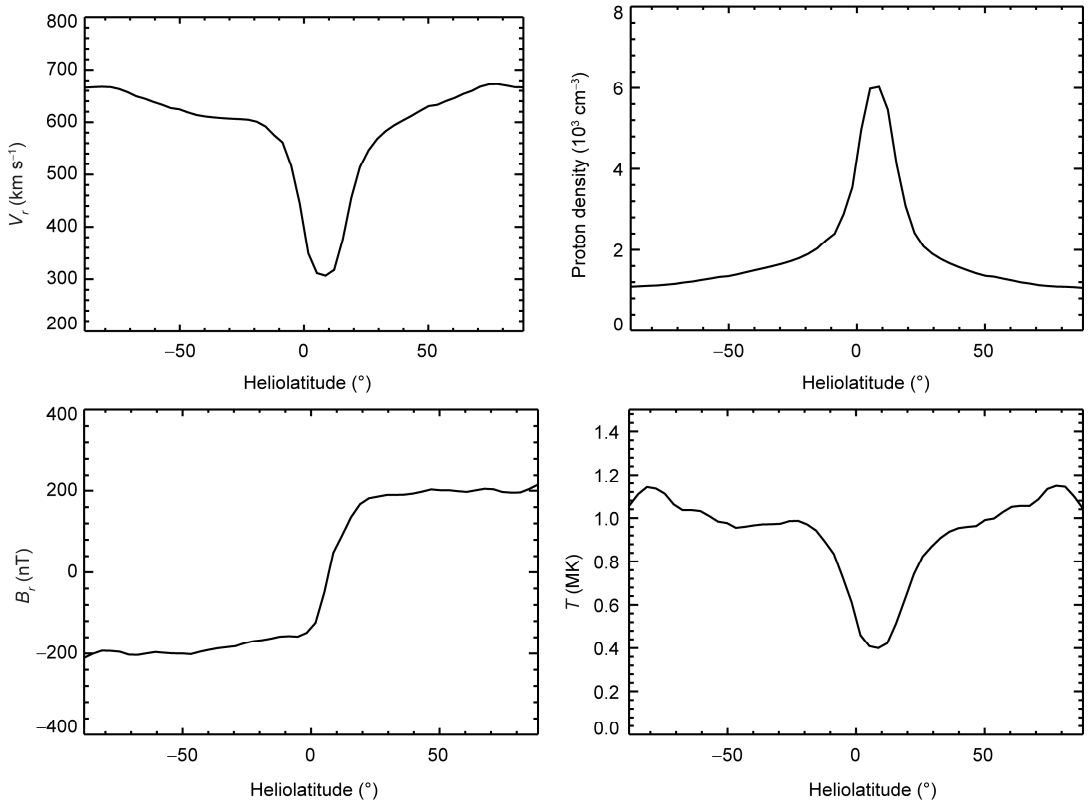

Figure 14 Profiles of the radial velocity, number density, radial magnetic field, and temperature at $20R_s$ and $\phi = 0°$.

scheme has been validated by investigating the error norm convergence for the two benchmark problems. Meanwhile, we conduct a comparative study between the improved CESE scheme and the original CESE scheme. From the two tests above, numerical results verify that the improved CESE scheme can reduce the numerical errors and enhance the solution quality due to CFL disparity. A comparison with the original CESE scheme shows better resolution of the present scheme results. From the second test, we found that the original CESE scheme is overly dissipative when CFL number is less than 0.1, but the improved CESE scheme can still retain the solution quality.

For its application to the solar wind simulation, we also apply this improved CESE scheme to the steady state solution of the solar coronal streamer structure using the 1D Parker solar wind solution together with a dipole field topology and measured photospheric magnetic field as an initial condition. The result shows that a reliable numerical solution for a 2D steady state coronal structure with solar wind can be obtained, as verified by observations near solar minimum (Sheeley et al., 1997; Biesecker et al., 1999). In particular, the numerical results shown for 3D steady state

structure for CR 1922 exhibit many properties typical of coronal atmospheric observations near solar minimum and provide us with strong confidence in the current MHD code. To this extent, we conclude that this present scheme has been validated by the tests performed for 2D and 3D cases. Further improvement and application of this scheme to model disturbance propagation in the corona and in interplanetary space and other astrophysical MHD flow problems are left for future work.

This work was jointly supported by the National Basic Research Program of China (Grant No. 2012CB825601), the Knowledge Innovation Program of the Chinese Academy of Sciences (Grant No. KZZD-EW-01-4), the National Natural Science Foundation of China (Grant Nos. 41031066, 41231068, 41074121 & 41074122), and the Specialized Research Fund for State Key Laboratories. We thank the reviewers for their valuable comments.

Biesecker D A, Thompson B J, Gibson S E, et al. 1996. Synoptic Sun during the first whole sun month campaign: August 10 to September 8. J Geophys Res, 1999, 104: 9679–9689

Chang S C. 1995. The method of space-time conservation element and solution element—A new approach for solving the Navier-Stokes and Euler equations. J Comput Phys, 119: 295–324

Chang S C, Wang X Y. 2003. Multi-dimensional Courant number insensitive CE/SE Euler solvers for application involving highly non-uniform meshes. AIAA-2003-5285

Chang S C, Wang X Y, Chow C Y. 1994. New developments in the method of space-time conservation element and solution element—Applications to two-dimensional time-marching problems. NASA TM 106758

Chang S C, Wang X Y, Chow C Y. 1999. The space-time conservation element and solution element method: A new high resolution and genuinely multidimensional paradigm for solving conservation laws. J Comput Phys, 156: 89–136

Chen Y, Hu Y Q. 2001. A two-dimensional Alfvé-wave-driven solar wind model. Sol Phys, 199: 371

Davoudzadeh F, McDonald H, Thompson B E. 1995. Accuracy evaluation of unsteady CFD numerical schemes by vortex preservation. Comput Fluids, 24: 883–895

Feng X S, Hu Y Q, Wei F S. 2006. Modeling the resistive MHD by the CESE method. Sol Phys, 235: 235–257

Feng X S, Yang L P, Xiang C Q, et al. 2010. Three-dimensional solar wind modeling from the Sun to Earth by a SIP-CESE MHD model with a six-component grid. Astrophys J, 723: 300–319

Feng X S, Zhou Y F, Wu S T. 2007. A novel numerical implementation for solar wind modeling by the modified conservation element/solution element method. Astrophys J, 655: 1110–1126

Gosling J T, Borrini G, Asbridge J R, et al. 1981. Coronal streamers in the solar wind at 1AU. J Geophys Res, 86: 5438–5448

Gottlieb D, Turkel E. 1976. Dissipative two-four methods for time dependent problems. Math Comp, 30: 703–723

Hu Y Q, Li X, Habbal S R. 2003. A 2.5-dimensional MHD Alfvé-wave-driven solar wind model. J Geophys Res, 108: 1378

Hundhausen A J. 1972. Coronal Expansion And Solar Wind. New York: Springer-Verlag

Jiang C W, Feng X S, Zhang J, et al. 2010. AMR simulation of magnetohydrodynamic problems by the CESE method in curvilinear coordinates. Solar Phys, 267: 463–491

Jiang G S, Wu C C. 1999. A high-order WENO finite difference scheme for the equations of ideal magneto-hydrodynamics. J Comput Phys, 150: 561–594

Li B, Li X, Hu Y Q, et al. 2004. A two-dimensional Alfvé-wave-driven solar wind model with proton temperature anisotropy. J Geophys Res, 109, doi: 10.1029/2003JA010313

Orszag A, Tang C M. 1979. Small-scale structure of two-dimensional magnetohydrodynamic turbulence. J Fluid Mech, 90: 129–145

Pneuman G W, Kopp R A. 1971. Gas-magnetic field interactions in the solar corona. Sol Phys, 18: 258–270

Qamar S, Mudasser S. 2010. On the application of a variant CE/SE method for solving two-dimensional ideal MHD equations. Appl Numer Math, 60: 587–606

Sheeley N R J, Wang Y M, Hawley S H, et al. 1997. Measurements of flow speeds in the corona between 2 and 30 solar radii. Astrophys J, 484: 472–478

Steinolfson R, Suess S T, Wu S T. 1982. The steady global corona. Astrophys J, 255: 730–742

Venkatachari B S, Cheng G C, Soni B K, et al. 2008. Validation and verification of Courant number insensitive CE/SE method for transient viscous flow simulations. Math Comput Simulat, 78: 653–670

Wang A H, Wu S T. 1993. A two-dimensional MHD global coronal model-steady-state streamers. Sol Phys, 147: 55–71

Wang X Y, Chang S C. 1999. A 2D non-splitting unstructured triangular mesh Euler solver based on the space-time conservation element and solution element method. Comp Fluid Dynam J, 8: 309–325

Wang X Y, Chow C Y, Chang S C. 1995. Application of the space-time conservation element and solution element method to two-dimensional advection-diffusion problems. NASA TM 106946

Wei F S, Feng X S, Cai H C, et al. 2003. Global distribution of coronal mass outputs and its relation to solar magnetic field structures. J Geophys Res, 108: A6, 1238, doi:10.1029/2002JA009439

Yee H C, Sandham N D, Djomehri M J. 1999. Low-dissipative high-order shock capturing methods using characteristic-based filters. J Comput Phys, 150: 199–238

Yen J C, Duell E G, Martindale W. 2006. CAA using 3D CESE method with a simplified Courant number insensitive scheme. AIAA 2006–2417

Yen J C, Wagner D A. 2005. Computational aeroacoustics using a simplified Courant number insensitive CE/SE method. AIAA 2005–2820

Zhang J H, Wei F S. 1993. The interaction between the solar fluid and magnitic field in the meridian plane. Sci China Ser A-Math, 23: 427–436

Zhang M, Yu S T, Chang S C. 2002. A space-time conservation element and solution element method for solving the two-dimensional unsteady Euler equations using quadrilateral and hexahedral meshes. J Comput Phys, 175: 168–199

Zhang M J, Yu S T, Lin S C. 2003. Calculation of the ideal MHD equations by the CE/SE method without special treatment for the divergence-free constraint of magnetic field. AIAA 2003–0324

Zhang M J, Yu S T, Lin S C, et al. 2006. Solving the MHD equations by the space-time conservation element and solution element method. J Comput Phys, 214: 599–617

Zhou Y F, Feng X S, Wu S T, et al. 2012. Using a 3-D spherical plasmoid to interpret the Sun-to-Earth propagation of the 4 November 1997 coronal mass ejection event. J Geophys Res, 117: A01102, doi: 10.1029/2010JA016380